Retrieval of Kinematic Fields from Dual-Beam Airborne Radar Data Gathered in Circular Trajectories during the FASTEX Experiment

G. SCIALOM, A. PROTAT, AND Y. LEMAÎTRE

Centre d'étude des Environnements Terrestre et Planétaires, Velizy, France

(Manuscript received 22 April 2002, in final form 16 October 2002)

ABSTRACT

The present paper describes the vertical structure of the wind field obtained by analysis of ''purls,'' that is, circular trajectories regularly performed by airborne dual-beam Doppler radars within the FASTEX frontal cyclones. Kinematic information on these systems are obtained using a new analysis scheme named DAVAD (Dual-Beam Antenna Velocity Azimuth Display). Using this scheme, it is possible to obtain the mesoscale wind field and its first-order derivatives, that is, the horizontal divergence (thus the vertical velocity), the stretching and shearing deformations, and the vertical component of vorticity. A unique advantage of this analysis is that it also provides a direct estimate of the terminal fall velocity of the hydrometeors. All these parameters are crucial for validation and initialization of mesoscale and large-scale models. The capabilities of this method and the best conditions for its application are assessed through simulations. Finally, an example of application of the scheme on the secondary low observed during the Fronts and Atlantic Storm Track Experiment (FASTEX) Intensive Observation Period (IOP) 12 is discussed. Results of purl processing using DAVAD are being included in the FASTEX database.

1. Introduction

Since the beginning of modern meteorology, the description of the dynamical structure and organization of precipitating systems is a problem of crucial interest. This interest has been progressively evolving from the large-scale and convective-scale motions toward mesoscale motions on the one hand, and to the scale interactions on the other hand. The feedback between current theory, experiment, and modeling, along with the crucial role of the mesoscale phenomena, has initiated a considerable development of radar systems, and in particular, airborne radar systems, which are systems particularly suited to this scale and to observing precipitation over oceans. Airborne radars with single-beam antennas were first developed (Jorgensen et al. 1983), followed by systems equipped with dual-beam antennas (Hildebrand et al. 1994). Moreover, in addition to the development of new instrumentation, considerable efforts have been devoted to modeling.

The international field experiment Fronts and Atlantic Storm-Track Experiment (FASTEX) had both experimental and modeling scientific objectives (Joly et al. 1997). This experiment, devoted to frontal waves and the frontal cyclogenesis in the Atlantic Ocean, took place in January–February 1997. During the FASTEX campaign, considerable experimental means associated with forecasting were deployed throughout the Atlantic Ocean, while a great effort was made in the coupling of experimentally derived meteorological fields with models. The building of a FASTEX database, which is one of the main objectives of the experiment, is intended to allow this coupling by documenting the observed phenomena (within frontal waves and secondary lows) by meteorological fields obtained through data analysis in view of model validation and initialization.

An example of such fields is the vertical structure of the wind field obtained by analysis of the ''purls'', that is, circular trajectories performed by the airborne dual-beam Doppler radars monitored during FASTEX. Such purls were regularly performed along the straight lines flown by the aircraft within the FASTEX frontal cyclones. Performing purls all along the experiment allows the mesoscale wind field and fields of related parameters (vertical vorticity, divergence, deformation, terminal fall velocity of the hydrometeors) to be retrieved on a regular basis. Purl processing was done using a new analysis scheme named Dual-Beam Antenna Velocity Azimuth Display (DAVAD).

DAVAD is derived from the classical Velocity Azimuth Display (VAD) analysis of ground-based radar data, which relies upon conical scannings, and upon the hypothesis that the horizontal wind components are linear in terms of the horizontal coordinates (Browning and Wexler 1968; Testud et al. 1980; Srivastava et al.

Corresponding author address: G. Scialom, CETP-CNRS-UVSQ 10-12, Avenue de l'Europe, 78140 Vélizy, France.
E-mail: scialom@cetp.ipsl.fr

1986; Matejka and Srivastava 1991). The VAD analysis was adapted to dual Doppler radar scanning by Scialom and Testud (1986) under the name of DVAD analysis. The VAD–DVAD ensemble was first adapted to single-beam airborne radars performing purls, an adaptation that is straightforward but requires that many specific problems be solved, as pointed out by Protat et al. (1997). This method was implemented under the name of SAVAD analysis (single or double SAVAD, depending on the number of radars), and applied to the data of TOGA–COARE (Tropical Ocean Global Atmosphere–Coupled Ocean Atmosphere Response Experiment; Webster and Lucas 1992). If the airborne Doppler radar is dual-beam, the geometry of observation is slightly different. In this context, DAVAD is an adaptation of single SAVAD to a dual-beam geometry and thus allows the retrieval of the 3D wind field and the associated physical parameters from the data gathered during the purls, and in particular of the vertical component of the vorticity, which is an advantage with respect to the single SAVAD. Note that purls (either with single or dual-beam antenna) were first extensively exploited during the TOGA–COARE experiment by Mapes and Houze (1995) who analyzed statistically the divergence profiles obtained throughout the experiment within these circular trajectories. They took advantage of (i) the short duration of purls, thus mitigating the effects of advection and internal evolution; (ii) the short ranges, which minimize the effects of beam widening and attenuation, and of sea clutter contamination. Contrarily to Mapes and Houze method, in DAVAD, the global volume is processed in order to retrieve not only the divergence profile, but also the other crucial kinematic parameters mentioned previously. Moreover, in the DAVAD approach, the vertical profiles of horizontal divergence, mean vertical velocity and vertical vorticity are retrieved simultaneously through a linear regression allowing a separation of these three parameters, as specified in section 2b(1). No assumption is thus needed for the value of the hydrometeor fall speed.

In section 2 of the present paper, the principle and mathematical formulation of the DAVAD analysis are detailed. In section 3, the main results of the performed simulations are given in order to test the sensitivity of the method to effects of the various technical parameters of the aircraft, of the radar and of the radar sequence, in particular the radar noise, the data resolution in terms of elevation and azimuth, and the radius of the purl. These simulations were particularly relevant in the context of FASTEX since their results were taken into account when achieving the final design of this experiment. The application of the method to Intensive Observation Period (IOP) 12 extracted from the FASTEX dataset is given in section 4, along with elements of interpretation of the derived 3D circulations.

2. Principle and mathematical formulation of the method

The present section is subdivided in two subsections in which the principle of the method (section 2a) and its refinements (section 2b) are successively developed. Indeed we shall see that if all the first-order derivatives of the wind can be theoretically obtained by a least squares approach, their accuracy can be insufficient in real cases, and must be improved. Thus, since several determinations of them can be obtained, it seems natural to present a variational approach of the problem in order to improve the accuracy and/or to resolve the problem even in the case of partially available data.

a. Principle of the retrieval

Airborne Doppler radars have proved to be an essential tool in the field of radar meteorology, because of their ability to follow precipitating systems, in particular over oceans, and to get their time evolution. The first radars possessed a single-beam antenna, scanning perpendicular to the aircraft track, offering a single view of the sampled system (Jorgensen et al. 1983; Hildebrand and Mueller 1985). A second view (not colinear to the first one) allows, one using the continuity equation, to obtain the three-dimensional wind field. This can be achieved by performing two successive paths nearly perpendicular to each other; however one needs to assume stationarity of the observed system, and in any case the time resolutions degraded using this technique. This is the reason why Frush et al. (1986) proposed Fore–Aft Scanning Technique (FAST) scanning, in which the antenna is tilted with respect to the perpendicular to the track, offering a second viewing angle of the system. This idea was improved by developing dual-beam antennas, scanning respectively fore and aft of the aircraft track (Hildebrand et al. 1994). Two airborne radars with such antennas were deployed during FASTEX [i.e., the National Oceanic and Atmospheric Administration (NOAA) P3-43, and the U.S.–French ELDORA/ASTRAIA (Electra Doppler Radar–Analyse Stéréoscopique pour Radar à Impulsions Aéroporté) radar onboard the National Center for Atmospheric Research (NCAR) Electra aircraft]. An illustration of this scanning is given in Fig. 1 in the case of a circular trajectory. This figure shows both antennas (fore and aft) scanning circles. Without aircraft motion, the antennas would generate cones on which the black vertical circles would display the motion of a particular gate at a given range from the radar. Due to aircraft motion, the sampling is helical along the circular aircraft trajectory. In the following to simply expose the DAVAD method, we use notations, in particular for angles, close to that of ground-based Doppler radars and of VAD analysis. Of course, as indicated in Lee et al. (1994), the geometry of scanning in airborne radars needs several coordinate systems to be used, in order to take into

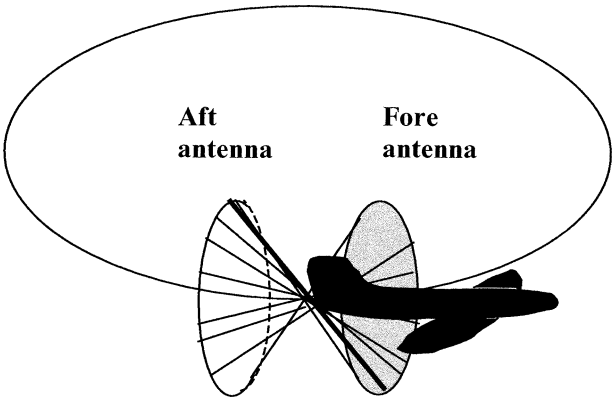

FIG. 1. Scans performed by the dual-beam antenna on an airborne Doppler radar flying a ''purl'' (circular trajectory). The vertical circles display the trajectory that a gate at a given range from the radar would follow without aircraft motion. Including the aircraft motion, these circles become helices.

account the aircraft navigation angles (roll, pitch, and drift) as provided by the Inertial Navigation System. Simulations performed in the following take these considerations into account. The effects of these angles are discussed in section 3g.

Let us consider one point M scanned successively by the fore and aft antennas (Fig. 2). The aircraft A flies along its circular trajectory on a horizontal plane at altitude z, where R is the radius of the circular trajectory, β is the azimuth of the measured point with respect to the north, β' is the azimuth of the aircraft (Fig. 2a), θ is the elevation of the measured point with respect to the horizontal plane (Fig. 2b), P is the projection of M onto the vertical plane perpendicular to the aircraft track (containing radius R), θ' is the elevation (Fig. 2b) of the measured plane PAM with respect to the horizontal plane, α is the tilt angle of each antenna fore and aft of the plane perpendicular to the aircraft track, r is the distance of the sampled point from the radar, and finally angle ξ is the projection of angle α on the horizontal. With the convention used in this paper for the winds, angles are counted positive clockwise from the north, and speeds are positive toward the antenna. We may write for an aircraft turning counterclockwise (Fig. 2a)

$$\beta' = \beta + \xi \tag{1}$$

for the fore antenna and

$$\beta' = \beta - \xi \tag{2}$$

for the aft antenna. Equations (1) and (2) are exchanged for an aircraft turning clockwise.

Considering the right triangles *AmM*, *ApP*, *APM*, and *Apm* (with right angles in *m*, *p*, *P*, and *m*, respectively), it becomes (Fig. 2b)

$$\cos\xi = \cos\theta' \cos\alpha/\cos\theta. \tag{3}$$

Let us first consider the fore antenna in Fig. 2b. The measured point being at distance r from the aircraft [r is positive (negative) for gates describing circles external (internal) to the aircraft purl], its coordinates (x to the east, y to the north) can be written as

$$x = R \sin\beta' + r \cos\theta \sin\beta \tag{4}$$

$$y = R \cos\beta' + r \cos\theta \cos\beta, \tag{5}$$

where the origin of the reference frame is point O on the vertical axis about which the aircraft performs its circular trajectory, and O is at altitude z of point M.

In the following, the presentation of the method will only concern external circles, that is, corresponding to gates toward the exterior of the purl. When considering internal gates, similar equations may be written, and taking account of internal gates presents no additional difficulty.

An implicit hypothesis made in radar meteorology is that the horizontal velocity of hydrometeors is that of the surrounding air, while the measured vertical hydrometeor velocity V_f is the sum of the vertical air velocity $-W$ and of the terminal fall velocity of the hydrometeors V_{f0}. Since $V_r(\beta)$ is the air particle speed measured along the viewing axis, and U and V are the horizontal wind components, we shall proceed as for the analysis from ground-based radars. We first write $V_r(\beta)$:

$$V_r(\beta) = -(U \sin\beta \cos\theta + V \cos\beta \cos\theta) + V_f(\beta) \sin\theta. \tag{6}$$

Note that the geometry of the scanning is different from that of a ground-based radar performing a conical scanning. Thus, in order to use an analysis derived from the VAD analysis, the data must be rearranged on cones in a way similar to that used in Protat et al. (1997) who consider the pseudo-conical scanning performed by a single-beam antenna.

As in the classical VAD analysis (Browning and Wexler 1968) at ground, we consider that the vertical air velocity is small with respect to the terminal fall velocity of the hydrometeors. As shown later, the vertical wind component neglected in (6) is computed by vertical integration of the continuity equation using the retrieved horizontal divergence, and this assumption is checked a posteriori. If the horizontal components of the wind are assumed to be linear, we may write, using (4) and (5),

$$U = U_0 + \frac{\partial U}{\partial x}(R \sin\beta' + r \cos\theta \sin\beta) + \frac{\partial U}{\partial y}(R \cos\beta' + r \cos\theta \cos\beta) \tag{7}$$

$$V = V_0 + \frac{\partial V}{\partial x}(R \sin\beta' + r \cos\theta \sin\beta) + \frac{\partial V}{\partial y}(R \cos\beta' + r \cos\theta \cos\beta), \tag{8}$$

where U_0 and V_0 are the horizontal components at point

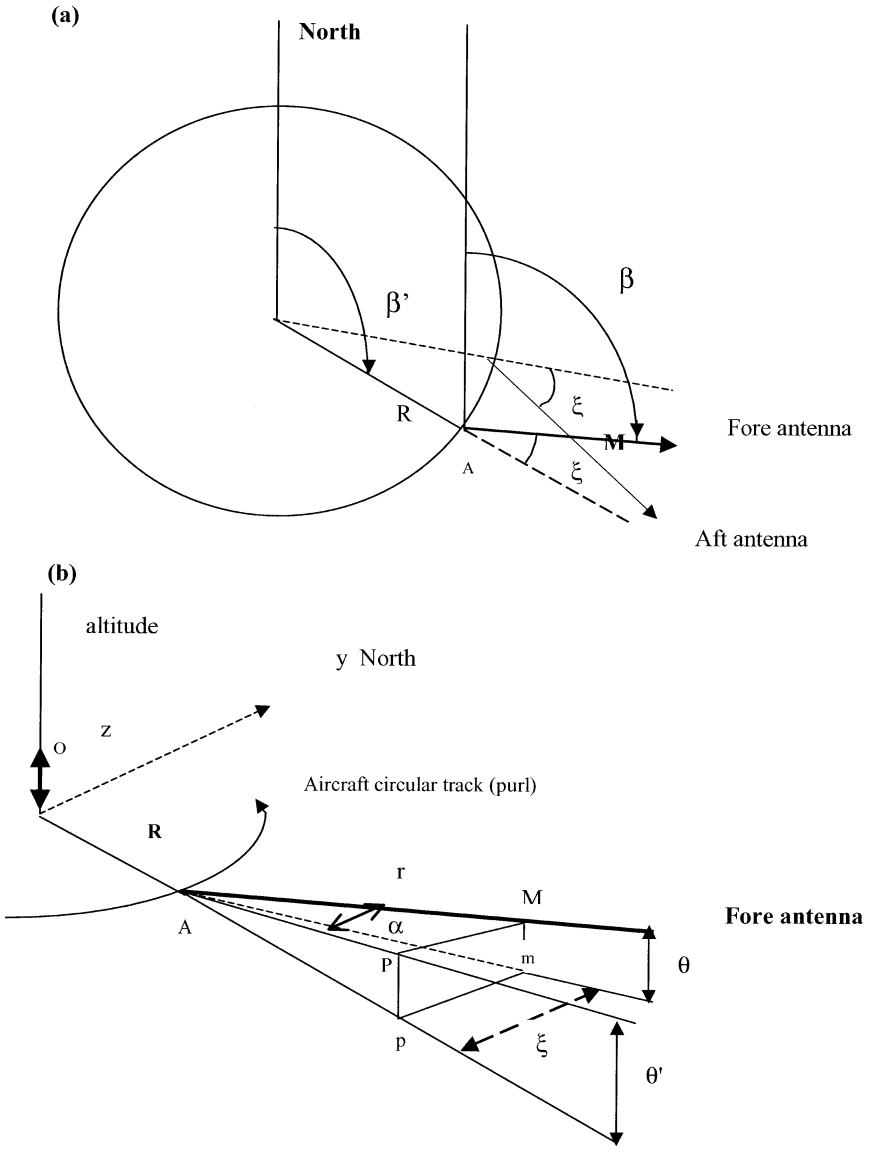

FIG. 2. Airborne Doppler radar flying a purl: (a) azimuth angles of the dual-beam antenna (view from top), and (b) elevation angles of the dual-beam antenna. The variable *M* is a point at distance *r* from the radar A successively seen by the fore and aft antennas; *P* is the projection of *M* onto the plane perpendicular to the aircraft trajectory; *m* and *p* are projections of *M* and *P* onto the horizontal, respectively; *R* is the purl radius; and *O* is the origin of horizontal axes at altitude *z* of *M*.

O (Figs. 2a,b), and $\partial U/\partial x, \ldots, \partial V/\partial y$ are the (assumed constant) horizontal derivatives of the horizontal components.

Combining (6), (7), and (8) and using (1) and (2) along a horizontal circle performed by a given gate at given range r and elevation θ, we may write $V_r(\beta)$ as a Fourier expansion up to order two as a function of azimuth β (as for the case of a ground-based radar):

$$V_r(\beta) = a_0 + a_1 \cos\beta + b_1 \sin\beta + a_2 \cos 2\beta + b_2 \sin 2\beta. \quad (9)$$

In a way similar to the case of ground-based radars, Fourier coefficients are computed (i) by least squares fitting of the theoretical expansion (9) to its experimental values on each of the horizontal circles described by each sampling gate during the aircraft purl, and (ii) by deriving the associated kinematic parameters from these Fourier coefficients (Testud et al. 1980).

Now consider both the fore and aft antennas. An additional index (f or a) is now necessary on a_i and b_i parameters and on related physical parameters to dis-

tinguish between information from the fore (a_{if}, b_{if}, . . .) and the aft (a_{ia}, b_{ia}, . . .) antennas.

The Fourier coefficients can be written as

$$a_{0f,a} = V_f \sin\theta - 0.5 \cos\theta(r \cos\theta + R \cos\xi)\text{DIV} - (\pm 0.5R \sin\xi \cos\theta\text{ROT}) \quad (10)$$

$$a_{1f,a} = -V_0 \cos\theta \quad (11)$$

$$b_{1f,a} = -U_0 \cos\theta \quad (12)$$

$$a_{2f,a} = 0.5 \cos\theta(r \cos\theta + R \cos\xi)\text{DET} - (\pm 0.5R \sin\xi \cos\theta\ \text{DES}) \quad (13)$$

$$b_{2f,a} = -0.5 \cos\theta(r \cos\theta + R \cos\xi)\text{DES} - (\pm 0.5R \sin\xi \cos\theta\text{DET}), \quad (14)$$

where DIV ($=\partial U/\partial x + \partial V/\partial y$), ROT ($=\partial V/\partial x - \partial U/\partial y$), DET ($=\partial U/\partial x - \partial V/\partial y$), and DES ($=\partial V/\partial x + \partial U/\partial y$) are, respectively, horizontal divergence, vertical component of the vorticity vector (denoted as vertical vorticity in the following), and stretching and shearing deformations.

It can be seen from (10)–(14) that using a single antenna or a single viewing angle [which is equivalent to retaining only one of the signs + or − in the terms with ± of (10), (13), and (14)] does not allow for all parameters since the problem is underdetermined (five equations for seven unknowns, including V_f). In order to solve this problem, measurements from two antennas are required in order to obtain at least as many equations as unknowns (the case of V_f will be discussed further in the next section). When comparing with the formulation of the ground-based traditional VAD analysis, it is seen that for the airborne case, (i) coefficient a_0, which provides (after correcting for the fall velocity V_f) the horizontal wind divergence DIV, is now contaminated by the vertical vorticity ROT; (ii) terms a_1 and b_1 are unchanged; (iii) term a_2 (classically the stretching deformation DET) is now contaminated by the shearing deformation DES, while term b_2 (classically the shearing deformation) is now contaminated by the stretching deformation. These ''contaminating'' terms are the expressions in parentheses following the minus sign in Eqs. (10), (13), and (14) and are specific of the analysis of dual beam airborne radar data, while the other terms are similar to those obtained in the case of ground-based radars.

If both antennas have worked properly, adding and subtracting the two forms of (10) yields the divergence (with a contribution of the fall velocity) and the vorticity. Using (13) and (14) yields, respectively, the stretching deformation and the shearing deformation for each antenna. Nevertheless, we cannot combine results deduced from the fore and the aft antennas in the same way as it was done in the DVAD analysis from two ground-based radars: indeed, Eqs. (11)–(12) provide the horizontal components of the wind at the center vertical of rotation of the purl, but, contrary to the case of ground-based radars, this provides twice the same information. Thus with a dual-beam antenna, the procedure to retrieve the 3D mesoscale wind field consists of the following.

- Process the data separately from each antenna, compute a_{0f}, a_{0a}, a_{1f}, a_{1a}, b_{1f}, b_{1a}, a_{2f}, a_{2a}, b_{2f}, b_{2a} for each horizontal circle followed by each gate at given r and θ; thus, we derive directly U_0 from b_{1f} (b_{1a}), V_0 from a_{1f} (a_{1a}), DET, and DES from a_{2f} and b_{2f} (or from a_{2a} and b_{2a}); since data are supposed to be representative of nearly identical areas, it can be checked if U_0, V_0, DET, and DES derived from both antennas are almost equal. If this is the case, it provides some confidence in the results.
- Combine a_{0f} and a_{0a} in order to obtain DIV (contaminated by V_f) and ROT.
- Calculate the horizontal derivatives $\partial U/\partial x$, $\partial U/\partial y$, $\partial V/\partial x$, $\partial V/\partial y$, from DIV, DET, DES, and ROT.

This procedure is straightforward and leads to good accuracy on the horizontal wind components but to moderate accuracy on the horizontal derivatives although the Fourier coefficients are accurate (which is not true in the present case as developed in section 3). Thus, in order to improve this accuracy, the equations are processed using a variational approach, as detailed in the next section.

The vertical air velocity W is obtained by integrating the continuity equation (or mass conservation) by steps along the vertical using the horizontal divergence DIV at each altitude and starting from the ground (with the boundary condition that W is zero at the ground). This integration process does not differ from that of the VAD and SAVAD analyses. Error on W increases with height since W is built by adding ΔW variations calculated at each altitude slice starting from the ground and going upwards. In particular, due to the lack of measurements at lower heights, there is a systematic error (some cm s^{-1}) on W. This error would be larger in convective cases.

b. Mathematical formulation of the problem and variational approach

The previous section discusses how the Fourier coefficients are derived from the processing of the radial winds for each radar gate. This processing is the first step of the DAVAD analysis. As shown in section 2a, the horizontal wind components and their first order derivatives can be derived from various combinations of the Fourier coefficients, but with only moderate accuracy since in real cases, for each gate and each elevation, there are at most 18 data points in the case of the P3-43 radar and 36 data points in the case of ELDORA-ASTRAIA radar, which is not sufficient to efficiently reduce the impact of radar noise. Thus in a second step, data from the first step are merged in several altitude slices and processed as a function of ele-

vation, which results in an increase of the amount of data and better accuracy of the retrieved wind parameters.

1) CALCULATION OF DIV, ROT, AND V_f FROM a_0 COEFFICIENT

This coefficient a_0 contains contributions from DIV, ROT and V_f. As seen in section 2a, the respective contributions from ROT and DIV "contaminated" by V_f are separated in a first step for each gate by combining a_{0f} and a_{0a} using (10):

$$V_f \sin\theta - 0.5 \cos\theta(r \cos\theta + R \cos\xi)\text{DIV} = 0.5(a_{0f} + a_{0a}) \quad (15)$$

$$\text{ROT} = -(a_{0f} - a_{0a})/R \sin\xi \cos\theta. \quad (16)$$

The second step is similar to the traditional VAD analysis. It consists of separating quantities that could not be directly obtained, such as DIV and V_f, and on the other hand, improving the accuracy of V_f, DIV, and ROT by processing as many data as possible in order to decrease the influence of the noise.

In what follows we describe this step in detail for the processing of a_{0f} and a_{0a} coefficients. The same procedure is used for the other Fourier coefficients. We merge the sets of (a_{0f}, a_{0a}) in altitude slices 300 m thick. These datasets correspond to various elevations θ_i and radial distances r_i. We assume that DIV, V_f, and ROT are constant in each altitude layer i. Instead of solving (15) and (16) directly for all measurements which would lead to an overdetermined system, we use a variational procedure in which Eqs. (15) and (16) must be approximately satisfied for the l available measurements of both a_{0f} and a_{0a} in each altitude layer i. This leads to minimization with respect to the unknowns DIV, V_f, and ROT, and the following expressions P_1 and P_2,

$$P_1 = \sum \lambda_l\{[(a_{0f} + a_{0a})/\sin\theta] - 2V_f + \text{DIV}[r \cos\theta(r \cos\theta + R \cos\xi)/r \sin\theta]\}^2 \quad \text{minimum} \quad (17)$$

$$P_2 = \sum \lambda_l\{[-(a_{0f} - a_{0a})] - R \sin\xi \cos\theta\text{ROT}\}^2 \quad \text{minimum;} \quad (18)$$

in which sums Σ are over l measurements on each altitude layer i.

Thus, ROT, DIV, and V_f are estimated through a least squares fitting procedure leading to

$$V_f = \frac{-0.5\left[\left(\sum \lambda_l x_l^2\right)\sum(\lambda_l y_l) - \sum(\lambda_l x_l)\sum(\lambda_l y_l x_l)\right]}{\left(\sum \lambda_l x_l\right)^2 - \sum(\lambda_l)\sum(\lambda_l x_l^2)} \quad (19)$$

$$\text{DIV} = \frac{-2\left[\sum(\lambda_l x_l)\sum(\lambda_l y_l) - \sum(\lambda_l)\sum(\lambda_l y_l x_l)\right]}{\sum(\lambda_l x_l)^2 - \sum(\lambda_l)\sum(\lambda_l x_l^2)} \quad (20)$$

$$\text{ROT} = \frac{-\sum(\lambda_l y_l' x_l')}{\sum(\lambda_l x_l'^2)}, \quad (21)$$

with $x_1 = 2[\cos\theta(r \cos\theta + R \cos\xi)/\sin\theta]$; $y_1 = (a_{0f} + a_{0a})/\sin\theta$; $x_1' = R \sin\xi \cos\theta$; $y_1' = (a_{0f} - a_{0a})$; and where λ_1 is a weighting factor automatically determined from the error matrix of the Fourier coefficients. This factor results from errors on Fourier parameters (thus indirectly from errors on measurements) and quantifies the expected accuracy of the retrieved quantities (DIV, ROT, and V_f).

2) a_1 AND b_1 COEFFICIENTS

The coefficients a_1 and b_1 are, respectively, related to V_0 and U_0. The procedure for their retrieval in each gate is similar to that used in the traditional VAD analysis. The estimate can also be improved by a least squares fitting procedure and a variational approach using (11) for V_0, and (12) for U_0, respectively:

$$P_1 = \sum_{lf} \lambda_{lf}[(a_{1f} + V_0 \cos\theta)]^2 + \sum_{la} \lambda_{la}[(a_{1a} + V_0 \cos\theta)]^2 \quad \text{minimum}$$

$$P_2 = \sum_{lf} \lambda_{lf}[(b_{1f} + U_0 \cos\theta)]^2 + \sum_{la} \lambda_{la}[(b_{1a} + U_0 \cos\theta)]^2 \quad \text{minimum,}$$

where λ_{lf} and λ_{la} are weighting factors, and Σ_{lf} and Σ_{la} are extended to lf and la circles, respectively, corresponding to the fore and aft antenna. This in turn leads to

$$U_0 = -\frac{\sum(\lambda_{lf} b_{1f} \cos\theta)}{\sum(\lambda_{lf} \cos^2\theta)} - \frac{\sum(\lambda_{la} b_{1a} \cos\theta)}{\sum(\lambda_{la} \cos^2\theta)} \quad (22)$$

$$V_0 = -\frac{\sum(\lambda_{lf} a_{1f} \cos\theta)}{\sum(\lambda_{lf} \cos^2\theta)} - \frac{\sum(\lambda_{la} a_{1a} \cos\theta)}{\sum(\lambda_{la} \cos^2\theta)}. \quad (23)$$

3) a_2 AND b_2 COEFFICIENTS

Both coefficients a_2 and b_2 include contributions from DET and DES. In the present case, several sets of equations are solved in order to retrieve DET and DES. As in section 2b(1), the problem is generally overdetermined and the estimates are improved using a variational procedure to take this overdetermination into account using Eqs. (13)–(14). Thus, we minimize the following cost functions with respect to DET and DES:

$$P_1 = \sum \mu_1(a_{2f} - x_2\text{DET} + y_2\text{DES})^2 + \sum \mu_2(b_{2f} + y_2\text{DET} + x_2\text{DES})^2 \quad \text{minimum}$$
$$+ \sum \mu_3(a_{2a} - x_2\text{DET} - y_2\text{DES})^2 + \sum \mu_4(b_{2a} - y_2\text{DET} + x_2\text{DES})^2 \quad \text{minimum.}$$

DET and DES are then given by the equations

$$\text{DET} = \frac{[\text{C1B2} - \text{C2B1}]}{[\text{A1B2} - \text{A2B1}]} \tag{24}$$

$$\text{DES} = \frac{[\text{C1A2} - \text{C2A1}]}{[\text{B1A2} - \text{A2B1}]}, \tag{25}$$

with

$$\text{A1} = (\mu_1 + \mu_3)\sum x_2^2 + (\mu_2 + \mu_4)\sum y_2^2 \tag{26}$$

$$\text{B1} = \text{A2} = (-\mu_1 + \mu_2 + \mu_3 - \mu_4)\sum (x_2y_2) \tag{27}$$

$$\text{C1} = \mu_1 \sum [a_{2f}x_2] - \mu_2 \sum [b_{2f}y_2] + \mu_3 \sum [a_{2a}x_2] + \mu_4 \sum [b_{2a}y_2] \tag{28}$$

$$\text{B2} = (\mu_1 + \mu_3)\sum y_2^2 + (\mu_2 + \mu_4)\sum x_2^2 \tag{29}$$

$$\text{C2} = -\mu_1 \sum [a_{2f}y_2] - \mu_2 \sum [b_{2f}x_2] + \mu_3 \sum [a_{2a}y_2] - \mu_4 \sum [b_{2a}x_2] \tag{30}$$

$$x_2 = 0.5\cos\theta(r\cos\theta + R\cos\xi) \tag{31}$$

$$y_2 = 0.5R\sin\xi\cos\theta \tag{32}$$

μ_1–μ_4 are weighting factors determined as in section 2b(1); Σ is as in section 2b(1).

3. Capabilities of the DAVAD analysis

In this section, a wind field is simulated in order to evaluate the accuracy of the method on the retrieval of wind and its first-order derivatives, and the sensitivity of the method to contaminating effects such as the radar noise, the data resolution and the radius of the purl. The simulated wind is assumed to vary linearly in the horizontal. In the first series of simulations, the wind has no vertical variations, and the vertical wind is set to zero. The simulated wind at the radar vertical has the following characteristics, with the notations of section 2:

$$U_0 = 10 \text{ m s}^{-1}; \qquad V_0 = -7 \text{ m s}^{-1};$$

$$\text{DIV} = \frac{\partial U}{\partial x} + \frac{\partial V}{\partial y} = 7.5 \times 10^{-5} \text{ s}^{-1};$$

$$\text{DET} = \frac{\partial U}{\partial x} - \frac{\partial V}{\partial y} = 1.25 \times 10^{-4} \text{ s}^{-1};$$

$$\text{DES} = \frac{\partial V}{\partial x} + \frac{\partial V}{\partial y} = 4.0 \times 10^{-5} \text{ s}^{-1};$$

$$\text{ROT} = \frac{\partial V}{\partial x} - \frac{\partial U}{\partial y} = 1.0 \times 10^{-4} \text{ s}^{-1};$$

$V_f = 7$ m s^{-1} below the 0°C isotherm (2000 m);

$V_f = 2$ m s^{-1} above the 0°C isotherm.

a. Software checking

The radius of the purl is 10 km, the aircraft flies at 360-m altitude (these parameters are not necessary realistic, they are just chosen for software checking). Data are simulated as regularly organized on successive cones with elevations θ from $-60°$ to $+60°$, with elevation resolution $\delta\theta$ (in °). On each cone, each gate from each antenna (fore and aft) describes a circle with azimuth resolution $\delta\beta$ (in °)—each circle is defined by $360/\delta\beta$ measurements. Let us recall (see section 2) that the wind retrieval consists of two steps: the first step is an analysis of the radial wind in each circle in terms of Fourier coefficients, and the second is an analysis of the Fourier coefficients by altitude slices in order to retrieve the wind components, horizontal divergence, deformation terms, and vertical vorticity. The altitude slice is set to 300 m thick.

The simulation of the wind field previously defined without noise, with $\delta\beta = 1°$ and $\delta\theta = 0.5°$, leads to perfect recovery of the simulated wind; that is, the software checks out within errors of the order 1×10^{-6} m s^{-1} for U_0, V_0, 10^{-10} s^{-1} for $\partial U/\partial x$, $\partial V/\partial x$, $\partial U/\partial y$, $\partial V/\partial y$, and 2×10^{-5} m s^{-1} for V_f.

b. Effect of the noise

If a Gaussian white noise 1.5 m s^{-1} standard deviation is added to the simulated radial wind (this noise is typical of airborne radars), the accuracy of the retrieved parameters depends on the elevation resolution retained for the analysis.

For an elevation range of $-60°$ to $+60°$ in 0.5° increments, and an azimuthal resolution of $\delta\beta = 1°$, the results are of the order 1×10^{-3} m s^{-1} for U_0, V_0, 10^{-7} to 10^{-8} s^{-1} for $\partial U/\partial x$, $\partial V/\partial x$, $\partial U/\partial y$, $\partial V/\partial y$, 2×10^{-3} m s^{-1} for V_f and are still very accurate. Nevertheless, the real data resolution is much lower than this one as discussed in the next paragraph.

c. Effect of the data resolution

In this section, we study the effect on the wind retrieval of the data resolution and of the elevation range on simulated data including a noise 1.5 m s^{-1} standard deviation.

i) For an elevation range of $-60°$ to $+60°$ in 2° increments, and an azimuthal resolution of $\delta\beta = 3°$, the results are of the order 2×10^{-2} m s^{-1} for U_0, V_0, 10^{-6} to 10^{-7} s^{-1} for $\partial U/\partial x$, $\partial V/\partial x$, $\partial U/\partial y$, $\partial V/\partial y$, 2×10^{-2} m s^{-1} for V_f and are satisfactory.

ii) If the azimuth resolution is degraded down to $\delta\beta = 15°$, then the accuracy becomes 7×10^{-2} m s^{-1} for U_0, V_0, 10^{-5} to 10^{-6} s^{-1} for $\partial U/\partial x$, $\partial V/\partial x$, $\partial U/\partial y$, $\partial V/\partial y$, 7×10^{-2} m s^{-1} for V_f and are still satisfactory.

iii) If the elevation range is only $-20°$ to $+20°$ in 2° increments, and if the azimuth resolution is kept at $\delta\beta = 15°$, then the accuracy is not very different from that of case ii, that is, 1×10^{-1} m s^{-1} for U_0, V_0, 10^{-5} to 10^{-6} s^{-1} for $\partial U/\partial x$, $\partial V/\partial x$, $\partial U/\partial y$, $\partial V/\partial y$, except for V_f for which the error is around 0.25 m s^{-1}, which is attributed to the fact that high elevations are excluded in the analysis.

iv) If the elevation range is kept at $-20°$ to $+20°$ but is in 0.5° increments and if the azimuth resolution is only $\delta\beta = 60°$, then the accuracy is close to that of case iii, since the improvement of the resolution by a factor 4 on elevation is compensated by a degradation by the same factor on the azimuth resolution.

v) For the P3 radar in the conditions of the FASTEX experiment and for when data with a resolution in elevation 0.5°, the resolution in azimuth is at most 20°; that is, the processing of data from each circle to calculate the five Fourier coefficients is performed on at most, 18 data points. For an elevation range $-20°$ to $+20°$, the accuracy is then 0.05 m s^{-1} for U_0, V_0, 10^{-5} -10^{-6} s^{-1} for $\partial U/\partial x$, $\partial V/\partial x$, $\partial U/\partial y$, $\partial V/\partial y$, 0.15 m s^{-1}, for V_f. The accuracy for V_f can be improved up to 0.05 m s^{-1} when the elevation range is $-60°$ to $+60°$.

d. Effect of the radius of the purl and of the altitude of the aircraft

Three radii of the purl, R, were tested, namely 2.5, 5, and 10 km. The corresponding times to perform these purls increase from 3 min up to 12 min, respectively. There is no effect of R on the accuracy of the mean horizontal wind components because they are determined from (11)–(12) through $a_{1\,f,a}$ and $b_{1\,f,a}$. Errors on wind derivatives decrease when the radius increases [see (10), and (13)–(14)], in a way inversely proportional to the radius down to a limit of about 2×10^{-7} s^{-1}. For example, the relative error on ROT (which corresponds to the worst case since ROT is calculated from a residual factor) is 10% for $R = 10$ km, 20% for $R = 5$ km, 40% for $R = 2.5$ km. However, choosing $R = 10$ km corresponds to a purl duration of 12 min; this would either imply that a linear flight pattern 60 km long be suppressed during the aircraft flight (which would change the sampling strategy), or if not, that the total flight duration would increase too much regarding the flight aircraft range. Thus despite the moderate accuracy of the wind derivatives when using small radii, the tradeoff was to fly purls of diameter 3 km during FASTEX.

Four aircraft altitudes, Z_A, were also tested—namely, 0.36, 1.3, and 5 km—the parameters of the simulation being those of section 3c, test ii [elevation range $-60°$ to $+60°$ in 2° increments, and azimuth resolution $\delta\beta = 15°$]. Errors on wind components and their derivatives are not very dependent on Z_A, because changing Z_A does not change significantly the statistical distribution of elevations.

e. Retrieval of winds with vertical gradients

In realistic situations, winds vary, sometimes strongly, with height. In order to simulate such situations, the wind previously defined analytically has been retained, except that $\partial U/\partial y$ and $\partial V/\partial x$ change with height. So, instead of a single volumetric value S_1 for vertical vorticity ROT we simulate $S_1 = 10^{-4}$ [integer part(altitude/300) $-$ 3000] s^{-1} in order that a large set of (positive and negative) values for ROT be explored (ROT increases by 10^{-4} s^{-1} increments from -3×10^{-4} s^{-1} in the 0–300-m layer up to 8×10^{-4} s^{-1} in the 3300–3600-m layer). A similar variation S_2 ($S_2 = 0.4 \times 10^{-4}$ s^{-1}) is simulated for shearing deformation DES. It is permissible to work in this way, since with DAVAD like with VAD, the retrieval of the horizontal wind is performed in each horizontal plane (The vertical wind is then integrated vertically using the horizontal divergence obtained previously). The result is that ROT and DES are retrieved with an accuracy of about 5–6 $\times 10^{-4}$ s^{-1}, in agreement with the previous results.

f. Recovery of quadratic winds with vertical gradients

In real applications, winds can significantly depart from the assumption of linearity, so that the retrieval of the wind components as if they were linear may lead to errors. Retrieving such a wind through a method like DAVAD (or VAD) will linearize it, that is, provide mean values for the first order derivatives that should be linear, as was shown in Scialom and Lemaître (1994). Up to a certain threshold, nonlinearities will lead to acceptable errors. Beyond this threshold, we will consider DAVAD to be no more robust with respect to nonlinearities. Thus a quadratic wind was simulated in which the constant and linear terms are as in section 3e, while the second order derivatives terms are $\partial U^2/\partial x^2 = 5 \times 10^{-9}$ m^{-1} s^{-1}, $\partial^2 U/\partial x \partial y = 3 \times 10^{-9}$ m^{-1} s^{-1}, $\partial^2 U/\partial y^2 = -2 \times 10^{-9}$ m^{-1} s^{-1}, $\partial^2 V/\partial x^2 = 3.4 \times 10^{-9}$ m^{-1} s^{-1}, $\partial^2 V/\partial x \partial y = 1.23 \times 10^{-9}$ m^{-1} s^{-1}, and $\partial^2 V/\partial y^2 = -7.6 \times 10^{-9}$ m^{-1} s^{-1}, respectively. The simulations were performed first without noise, then with a gaussian or white noise ± 1.5 m s^{-1} standard deviation. Second order derivative terms lead to *additional* variations of the wind about 11 m s^{-1} at 50-km distance from the radar (4 m s^{-1} at 30-km distance), which can be thought of as strong nonlinearities. Without noise, errors on the retrieved set of wind parameters are essentially biases:

$$\Delta U_0 = 0.6 \text{ m s}^{-1}; \qquad \Delta V_0 = 0.25 \text{ m s}^{-1};$$

$$\Delta\text{DIV} = \Delta\text{DET} = 2.5 \times 10^{-5} \text{ s}^{-1};$$

$$\Delta\text{DES} = 4.0 \times 10^{-5} \text{ s}^{-1};$$

$$\Delta\text{ROT} = \frac{\partial V}{\partial x} - \frac{\partial U}{\partial y} = 2.0 \times 10^{-4} \text{ s}^{-1};$$

$$\Delta V_f = 1.2 \text{ m s}^{-1}.$$

The vertical component of vorticity and the terminal fall velocity suffer in this case strong errors while the other parameters are acceptable. This provides the limit for avoiding to use DAVAD, this is, when the terminal fall velocity begins to depart from values expected in stratiform areas. Previous results hold when adding the noise to the quadratic wind. So, as discussed previously, this indicates again that noise is well filtered out by the analysis.

g. Other sources of errors; in particular, navigation angles

In real cases, other factors must be taken in to account. As shown in Protat et al. (1997), the navigation angles—roll, pitch, and drift (see their Fig. 5)—suffer errors which in turn increase errors on the kinematic retrieved parameters. For example, an error on the roll contaminates the elevation angles θ and θ'. In the same way, pitch and drift errors contaminate both the elevation and azimuth angles. In addition, owing to aircraft drift, purls are not perfectly circular but look like ellipses (see Fig. 4), inducing variations of the purl radius up to 30% about its mean value. Protat et al. (1997) first study a systematic error of 1° (which is huge) on roll, pitch, and drift, and show that it results in maximum errors of about 2×10^{-5} m s^{-1} for DIV, DET, and DES, and 0.5 m s^{-1} for the horizontal wind retrieved by SAVAD. This is also the case for DAVAD. Moreover for DAVAD, the maximum error on ROT is 4×10^{-5} s^{-1} since ROT is obtained as a residual term. However, systematic errors are corrected in the preprocessing of the airborne Doppler radar data using the echo returned from the earth's surface (Testud et al. 1995). So the only remaining errors on navigation and pointing angles are fluctuation errors which are well filtered out by the processing. The error on DIV and ROT are 3×10^{-6} s^{-1} and 6×10^{-6} s^{-1}, respectively, for a noise with standard deviation 0.2° for the roll angle.

The final accuracy (including all the previous sources of errors but nonlinearities) on the retrieved parameters can be estimated as 0.2 m s^{-1} for U_0, V_0, 4×10^{-5} to 4×10^{-6} s^{-1} for $\partial U/\partial x$, $\partial U/\partial y$, $\partial V/\partial x$, $\partial V/\partial y$ (1.5×10^{-4} for ROT), 0.1 m s^{-1} for V_f.

In summary, the practical application of DAVAD in real cases must be done carefully due to the various sources of errors encountered in the data processing. It must be noted that although the retrieval of the wind components from coefficients a_1 and b_1 and of the stretching and shearing terms from coefficients a_2 and b_2 is relatively straightforward, this is not the case for DIV and V_f, on the one hand, and ROT on the other hand [see section 2b(1)]. ROT is calculated as a residual term [see Eq. (18)], the accuracy of which is lower. As for the main term in (17) from which DIV and V_f are retrieved, it has to be analyzed in terms of radial distance: effective determination of V_f must be done by retaining measurements at high elevations while DIV will be determined by selecting preferentially low-elevation measurements.

4. Analysis of the FASTEX IOP 12 purls using DAVAD

The performance of the DAVAD analysis was examined in section 3 using simulated data. The present section is devoted to an application of this analysis to real data. Owing to the fairly large number of purls performed during this IOP, the selected case is the secondary low sampled during FASTEX IOP 12. This low has been documented by Lemaître et al. (1999). Data were collected in the so-called Mesoscale Sampling Area of FASTEX (see the FASTEX Operations Plan; Jorgensen et al. 1996). The main experimental facilities for that study were the UK-C130 aircraft able to launch dropsondes, the French–U.S. ELDORA-ASTRAIA radar onboard the Electra aircraft, and the P3-42 NOAA aircraft Doppler radar equipped with the dual-beam French antenna. The two airborne Doppler radars performed various types of trajectories such as straight lines regularly interrupted by purls (FASTEX Operations Plan; Jorgensen et al. 1996). The straight lines allow multiscale description of the lows using the Mutiple Analytical Doppler (MANDOP) analysis (Scialom and Lemaître 1990; Dou et al. 1996), while mesoscale profiles of the wind and its first derivatives are derived from the purl processing, as shown previously. During this IOP12, only the P3-42 radar data were available. This IOP is the most explosive low deepening, roughly −54 mb in 24 hours (9 February 1997) observed during FASTEX. The overall synoptic description of this situation is given in Lemaître et al. (1999). The explosive pressure deepening is associated with the low 34A on which the measurements are conducted. The Meteosat satellite IR picture (Figs. 3a–d) shows the evolution of the synoptic situation between 1500 and 1800 UTC, with the explosive deepening of a secondary low and the progressive development of the so-called cloud head and a dry slot features, which are the main signatures of a frontal cyclone. The low 34A first moves northeastward at 40 m s^{-1}, deepens and then tracks toward Iceland. A conceptual scheme of the secondary low and associated circulation (as described in Browning et al. 1997) is given in Fig. 3e, describing the main flows involved in the internal dynamics, namely, the warm conveyor belt (WCB) the main part of which (W1) is parallel to the cold front while the branch W2 wraps

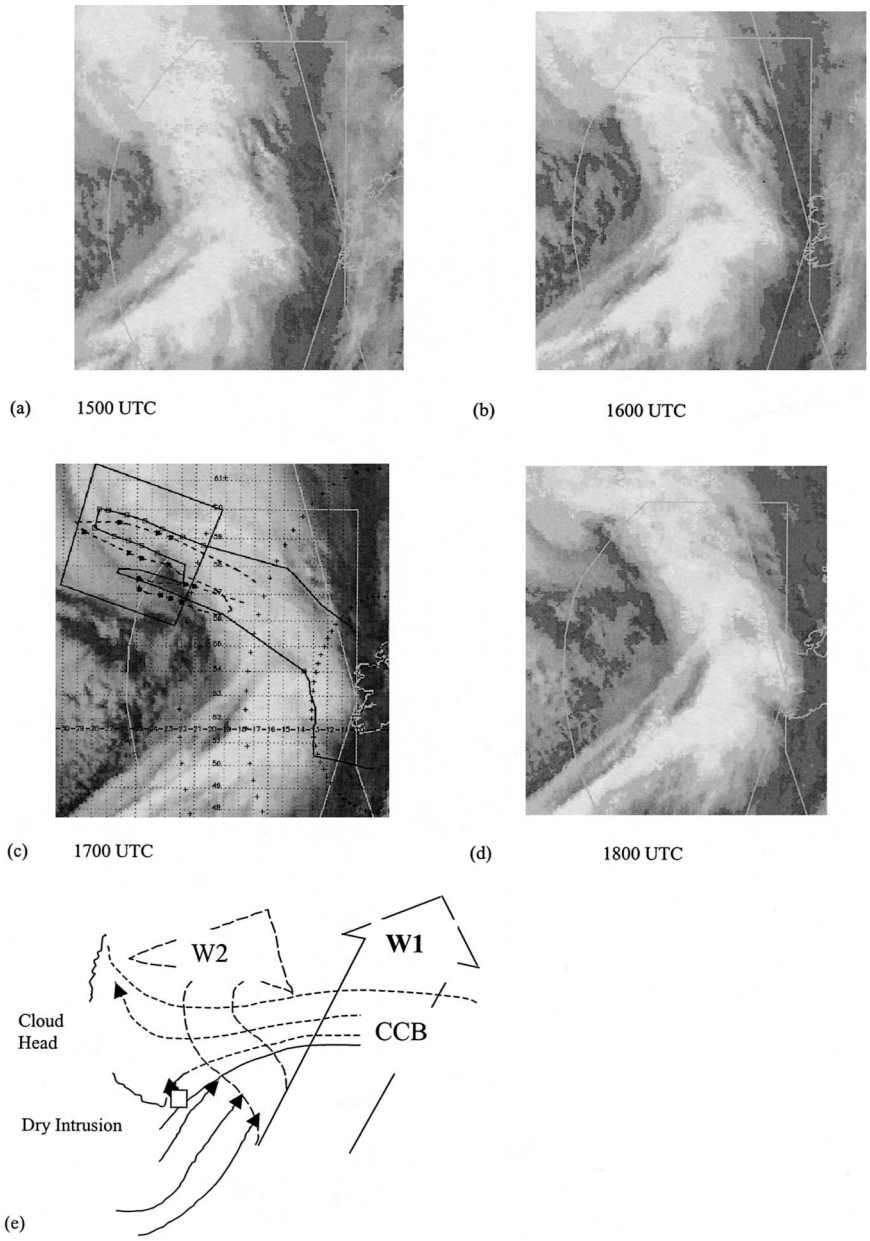

FIG. 3. Meteosat satellite IR picture at (a) 1500, (b) 1600, (c) 1700, and (d) UTC 1800, and (e) a conceptual scheme of the secondary low and associated circulation as proposed in Browning et al. (1997). Superimposed in (c) are the aircraft trajectory in the frame of reference linked to the whole precipitation area and the box for mesoscale retrieval using the MANDOP analysis (Lemaître et al. 1999).

around the frontal cyclone, the cold conveyor belt (CCB) along the secondary warm front associated with the secondary low. This low was sampled on the northwestern corner of the MSA. Figure 3c also shows the aircraft trajectory in the relative frame of reference linked to the sampled system. It can be seen that the secondary low has been crossed over by the P3-42 aircraft in order to sample the precipitating systems at several scales.

The box in Fig. 3c corresponds to the 430 km × 430 km area in which the mesoscale retrieval of the dynamics presented in Lemaître et al. (1999) was performed using the MANDOP analysis. In MANDOP, each component of the wind is expressed as the product of three functions, each of them being an expansion along an axis (*x*, *y*, or *z*, respectively) in series of orthogonal functions of a given base (e.g., Legendre polynomials, Fourier . . .) up to a given order, so that the radial wind along a given direction can also be expressed analytically. The analytical radial wind is then adjusted (in the

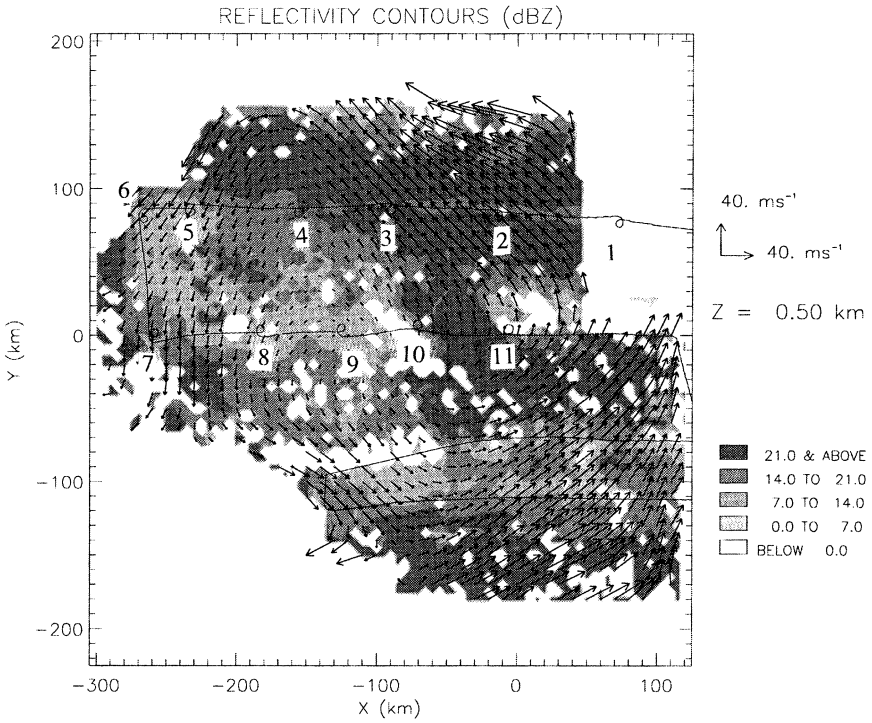

FIG. 4. Horizontal cross section of radar reflectivity and 3D absolute wind field at 0.5-km altitude as derived by Lemaître et al. (1999) using MANDOP. Superimposed is the aircraft track with the purls flown Numbers 1–11 refer to purls at 1531, 1544, 1557, 1609, 1625, 1634, 1645, 1659, 1709, 1720, and 1732 UTC, respectively.

least squares sense) to the experimental radial wind, for all experimental data in order to retrieve the coefficients of expansion of the wind. This process thus consists in solving a linear system, whose matrix is calculated using the orthogonal functions of the base. The system is generally ill-conditioned, since the vertical component of the wind is generally one order of magnitude less than the horizontal ones. So the continuity equation (or mass conservation) is also introduced in the process, along with a boundary condition, both expressed analytically under the form of matrices to be added to the main matrix of the problem. An important point concerns the scale selection: a given order of expansion corresponds to the scales retained in the analysis, so that smaller scales are filtered out. MANDOP presents numerous advantages associated with its analytical form—analytical form of physical parameters linked to the wind, possibility to process data from any source of radar data, both ground-based and airborne, . . . (see Scialom and Lemaître 1990 for more details)—but needs independent determination of the terminal fall velocity of hydrometeors. While under stratiform conditions, DAVAD, as seen in section 2, is able to provide it together with the vertical profile of the wind and associated first space derivatives. This is a decisive advantage of the present approach over the dual Doppler analyses, including MANDOP when one is interested in simple methods likely to be used under (quasi)-real time conditions. Moreover the terminal fall velocity vertical profile may help identify hydrometeors, and the wind vertical profile (including its first derivatives) may be used in assimilation schemes.

Figure 4 (adapted from Lemaître et al. 1999) shows the horizontal cross section of the 3D reflectivity and wind fields at 0.5-km altitude derived from the P3 tail-radar measurements. Figure 4 also displays the aircraft track, with the main purls flown along the track between 1500 and 1800 UTC. Note that during the 2 h of radar observations, the cyclone moved and evolved noticeably (Figs. 3a–d). However, since each purl lasts three minutes, it may be considered that advection and internal evolution do not affect individual profile calculations. As specified in Lemaître et al. (1999), three flows can be identified around the secondary low in Fig. 4, in agreement with the conceptual scheme of Browning et al. (1997): the CCB in the northern part of the figure (north of the convective band, with air at intermediate temperature); just south of this flow, the WCB that wraps around the frontal cyclone. The convective area around the cyclone is the east part of the cloud head. The flow in the northwest part is possibly of polar origin, and the flow in the southwest part is associated with the dry intrusion. The purls were mostly performed in the cloud head area as shown in Fig. 3. The wind pattern displayed in Fig. 4 suggests that the vorticity at mesoscale, is cyclonic at flight altitude in the secondary

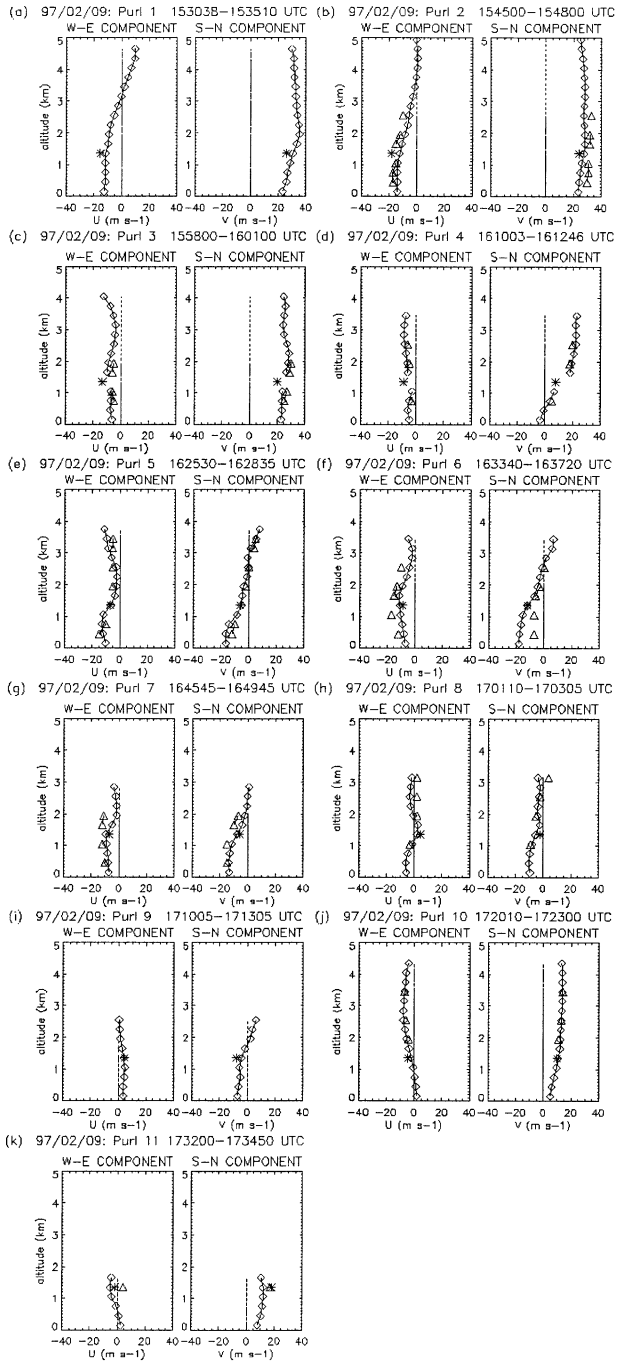

FIG. 5. Vertical profiles using DAVAD (diamonds) of the (left) W–E and (right) N–S horizontal components of the wind at (a) 1531, (b) 1544, (c) 1557, (d) 1609, (e) 1625, (f) 1634, (g) 1645, (h) 1659, (i) 1709, (j) 1720, and (k) 1732 UTC, respectively. Triangles are from MANDOP analysis, and asterisks are measurements from the wind sensor onboard the aircraft.

low area. We now turn to a description of the main results obtained with DAVAD.

Regarding the horizontal wind components using DAVAD [displayed Figs. 5a–k (left) W–E and (right) S–N components], three regimes are identified: the first one [Figs. 5a–c or purls 1–3] is mainly southerly and exhibits strong winds 25–35 m s^{-1} in magnitude in the lower troposphere, which is typical of the WCB area, then a northeasterly component appears first below 1-km altitude (Fig. 5f, purl 6) then up to 2–2.5 km [Figs. 5e–g, purls 5 and 7] and their magnitudes decrease; then they turn to be more northerly [Figs. 5h–i, purls 8 and 9], and finally turn southwesterly [Figs. 5j, k, purls 10 and 11]. The latter flow is typical of the dry intrusion area while the previous ones associated with the secondary low, are probably related to the CCB. The wind derived from DAVAD is in good agreement with the wind derived from the sensor onboard the aircraft and with the wind from MANDOP (see Fig. 5). Small discrepancies with MANDOP wind fields are due to the different conditions in which both analyses are applied: MANDOP analysis was applied in a whole area 430 × 430 km^2 at once on data gathered during two hours and correspond to scales resolved of around 20–30 km, while each purl processed independently with DAVAD is representative of a three minutes time lag, which corresponds to a larger scale of about 60 km.

The vertical profiles of the terminal fall velocity V_f in stratiform or moderately convective areas are generally characterized by values of about 5–12 m s^{-1} in rain, below the 0°C isotherm, and 0–2 m s^{-1}, in snow, above. In the present case, the eleven purls between 1530 and 1732 UTC show V_f profiles of similar shapes [see Figs. 6(a)–(k)], within the error bars (±0.1 m s^{-1}). On the same figure, each V_f profile is associated with a mean reflectivity profile.

Purls located in the northeastern part [Figs. 6(a)–(d), purls 1–4] exhibit stronger values in rain (6–8 m s^{-1}, associated with strong mean reflectivity values of 20–25 dBZ) than purls in the southern part of the domain (4–5 m s^{-1}; Figs. 6h–k, purls 8–11, characterized by lower mean reflectivities of around 15 dBZ). This suggests that strong evaporation occurs in the cloud head and dry air intrusion. Moreover the transition altitude between rain and snow is around 1000 m in the first case, 700 m in the second, which confirms that the air in the northeastern part is warmer (WCB) than the air in the southern part. Finally, a detailed examination of the V_f and reflectivity profiles above the 0°C isotherm (i.e., in solid precipitation) may in turn be split into a lower part with V_f velocity of about 2 m s^{-1} generally associated with a secondary reflectivity maximum, and an upper part, with V_f values ranging from 0 to 1 m s^{-1}, associated with lower reflectivities. This may be either the signature of a graupel layer overlaid by a snow layer or the signature of aggregation occuring (e.g., Locatelli and Hobbs 1974; Heymsfield 1978).

It must be noted that the consistent results obtained on the V_f profiles are an additional indirect a posteriori validation for the whole DAVAD analysis since V_f is the most difficult parameter to obtain.

Vertical profiles of vertical vorticity are displayed in Figs. 7(a)–(k). The vertical vorticity appears to be

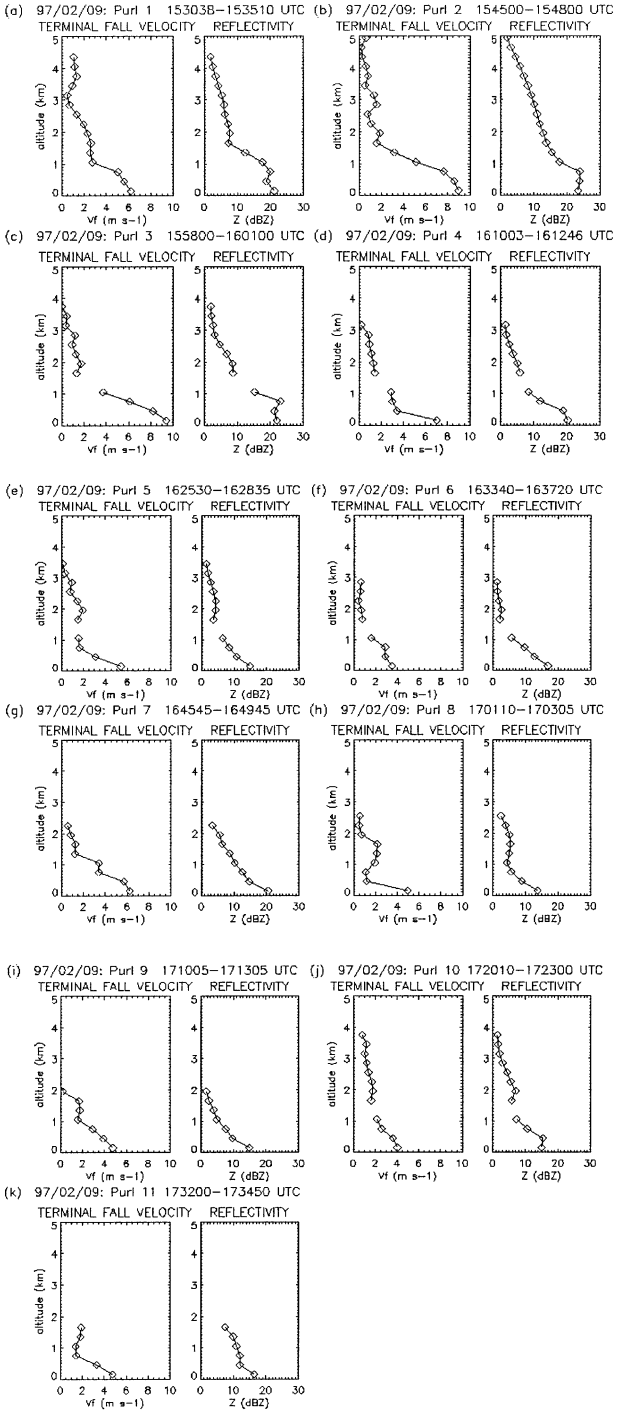

FIG. 6. Same as Fig. 5 for (left) terminal fall velocity and (right) reflectivity.

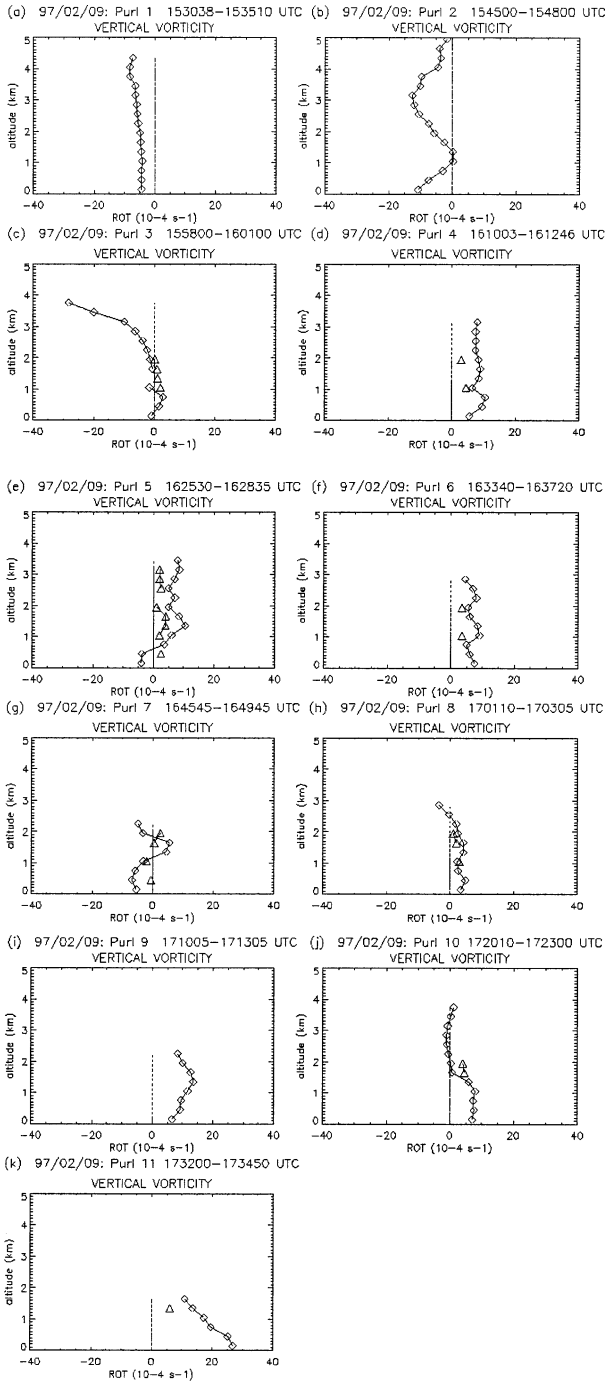

FIG. 7. Same as Fig. 5 for vertical vorticity.

positive—cyclonic, in the southern part of the domain, which is consistent with the existence of a secondary low [Figs. 7h–k, purls 8–11]. Values increase from 4 $\times$ 10^{-4} s^{-1}, at 1701 UTC to 25 $\times$ 10^{-4} s^{-1} at 1732 UTC. The vertical vorticity profile at 1732 UTC located within the low center corresponds to the absolute maximum of all purls at low levels, below 500-m altitude. This vorticity maximum also corresponds to a strong shearing deformation (Fig. 9k). In the northern part of the domain, vertical vorticity is generally negative (anticyclonic), consistent with the horizontal wind shear (Fig. 4), except at low altitudes at 1558 and 1610 UTC (Figs. 7c and d, purls 3 and 4, toward the low center) and between 1 and 2 km at 1701 UTC

(Fig. 7h close to the absolute maximum). Figure 7 also displays some MANDOP-derived vertical vorticity results. The comparison with the DAVAD results is generally good: the sign (generally positive, i.e., cyclonic) is preserved, but DAVAD vorticities are often greater than MANDOP vorticities, which may be attributed to the fact that, although the mean horizontal scale for DAVAD is greater, it also includes smaller-scale motions filtered out in MANDOP applied in such a large domain.

Vertical profiles of the vertical wind velocity obtained by upward integration of the horizontal wind divergence are displayed Figs. 8a–k. These profiles show that the vertical wind velocity is generally weak, in good agreement with the stratiform or moderately convective character of the precipitation, and also with the results of Lemaître et al. (1999) in which vertical motions are moderate. Note that as explained in section 2a, there is a systematic error ΔW (some cm s^{-1}) due to the lack of data at lower altitudes. Moreover vertical wind velocities are generally negative (subsiding) when located within anticyclonic areas. However, W is positive (ascending) at low altitude within the region of convergence between the WCB and the CCB (Fig. 8a), and within the vortex maximum at 1732 UTC (Fig. 8k), which is consistent with the current observation that cyclonic areas are also convergence areas. Vertical velocity is also positive between 1- and 2-km altitude at 1633 UTC in the cloud head region (Fig. 8f) in agreement with the analysis of particle trajectories of Lemaître et al. (1999).

The stretching and shearing deformations (Browning and Wexler 1968) also provide information on the dynamics of the flows [Figs. 9a–h]. Stretching dominates at 1530 and 1701 UTC below 1.5 km and 1732 UTC (Figs. 9a, h, and k). Shearing dominates at 1610, 1701, above 1.5 km and at 1710 above 0.5 km (Figs. 9d, h, and i). The other profiles show both shearing and stretching. The effect of these deformations on the horizontal potential temperature θ gradient can be estimated following Bluestein (1986), expressing the frontogenetic function F in terms of these deformations (denoted DET and DES) and of divergence DIV, tilting and diabatic function, and restricting the discussion to the adiabatic part of the frontogenesis:

$$F = D/Dt|\nabla_h\theta| = -0.5|\nabla_h\theta|(\text{DIV} - \text{DET}\cos 2\alpha_1 - \text{DES}\sin 2\alpha_1), \quad (33)$$

with α_1 the angle between the x axis (toward the east) and the baroclinic zone corresponding to the secondary low ($\alpha_1 = -30°$). Application of this equation to the present data leads to Figs. 10a–k, which exhibits frontogenetic terms due to deformation alone, and to deformation plus divergence (denoted as DEF FRONTOGEN and TOTAL FRONTOG, respectively, on the figures):

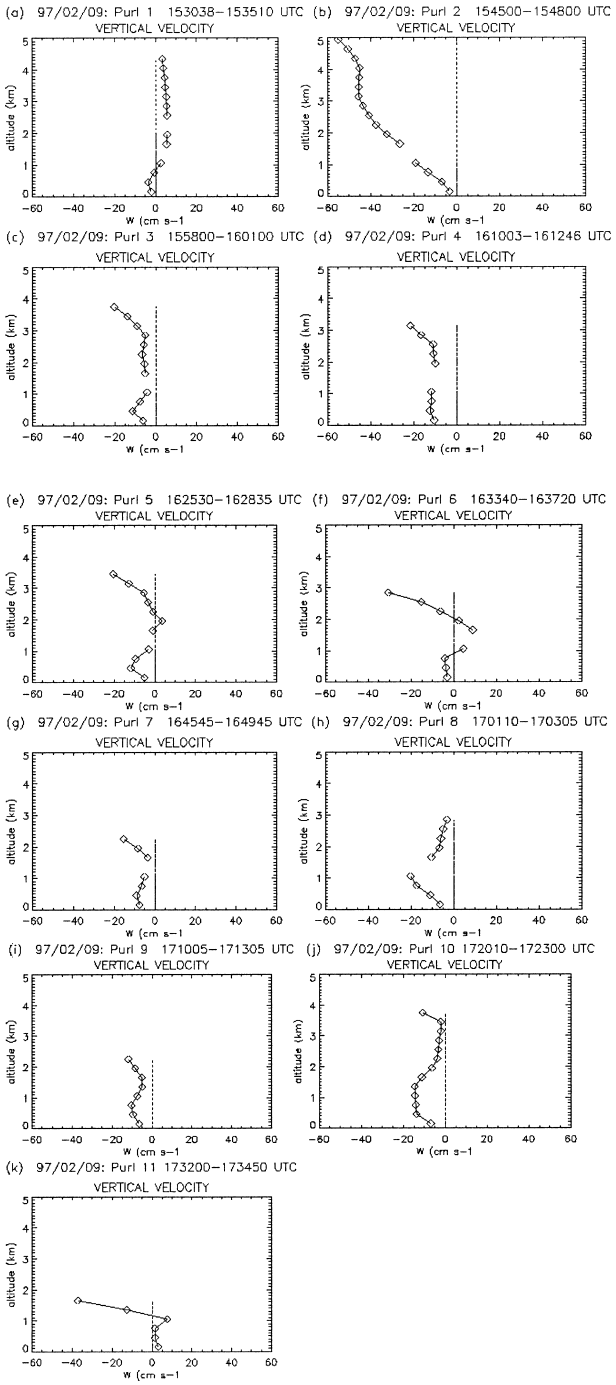

FIG. 8. Same as Fig. 5 for vertical velocity.

$$\text{DEF FRONTOGEN} = \text{DET}\cos 2\alpha_1 + \text{DES}\sin 2\alpha_1 \quad (34)$$

$$\text{TOTAL FRONTOG} = -\text{DIV} + \text{DET}\cos 2\alpha_1 + \text{DES}\sin 2\alpha_1. \quad (35)$$

Purls 2–5 are performed in frontolytic areas [Figs. 10b–e], while purls 8, 10, and 11 are rather within fronto-

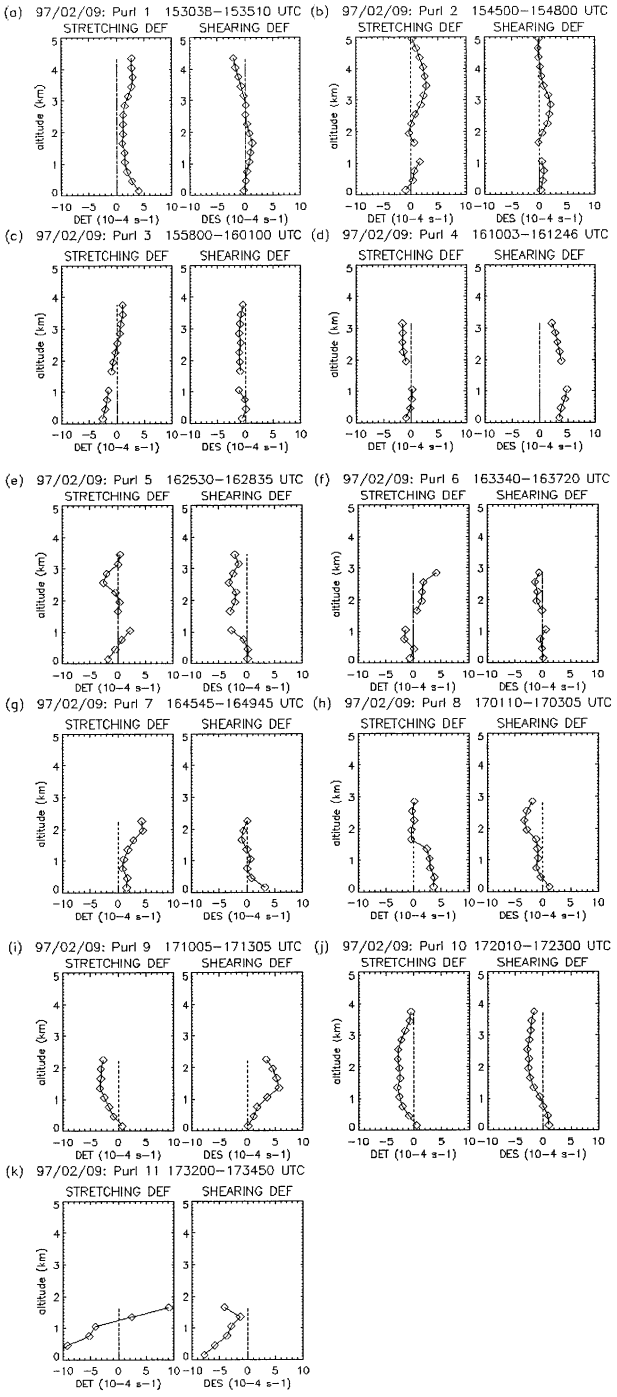

FIG. 9. Same as Fig. 5 for (left) stretching and (right) shearing deformations.

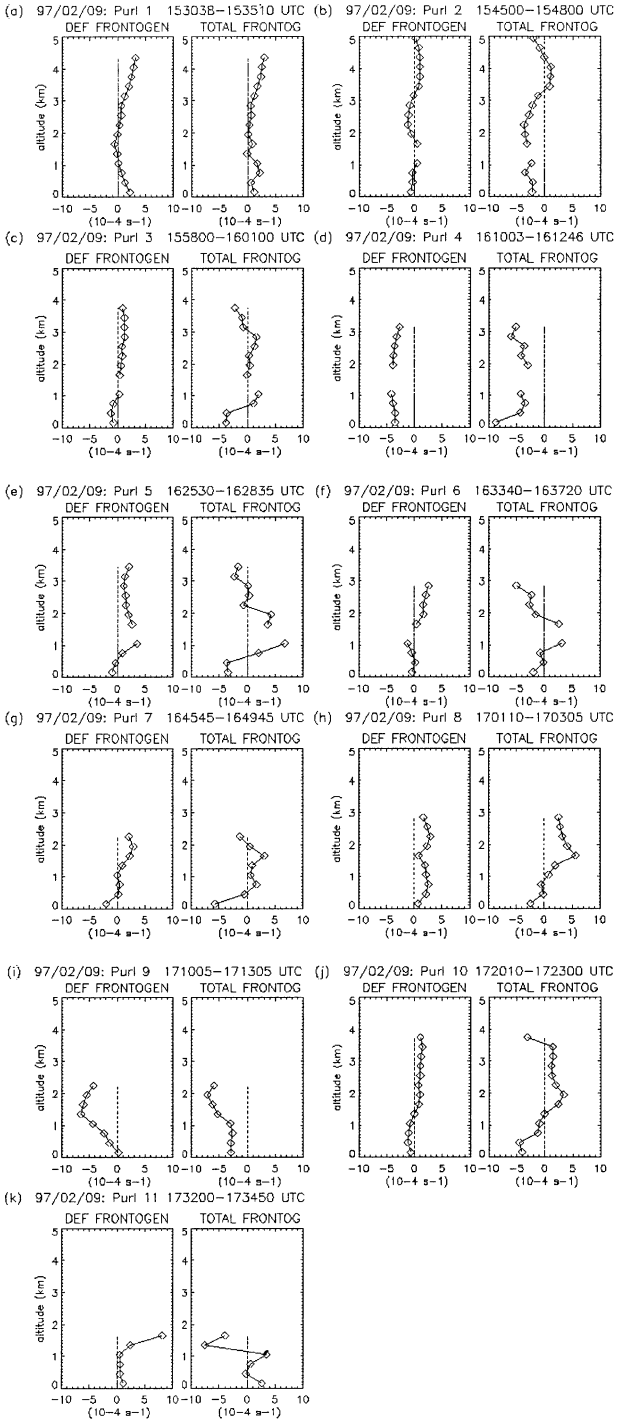

FIG. 10. Same as Fig. 5 for the frontogenetic terms due to (left) deformation alone, and to (right) deformation and divergence.

genetic areas (Figs. 10h, j, and k). The conclusion is that, in the active part of the cloud head, the observed stretching deformation is frontolytic (the stretching term of F is -4×10^{-4} K m^{-1} s^{-1}), and therefore tends to reduce the horizontal gradient of temperature, whereas on the western part of the cyclone, the observed shearing deformation tends to produce a new baroclinic zone (the shearing term of F is 3×10^{-4} K m^{-1} s^{-1}). These results are consistent with the temperature pattern retrieved by Lemaître et al. (1999) who found a relatively uniform field on the east side of the cloud head and a well-defined baroclinic region on its west side.

5. Conclusions

The DAVAD analysis described previously is devoted to the retrieval of the wind field, its divergence, deformations, and vertical vorticity, and the terminal fall velocity V_f within the stratiform area of convective precipitating systems. The analysis takes advantage of the VAD approach that it is derived from, since the data are rearranged in the same scanning geometry (conical). It benefits from the additional information brought by the two viewing angles under which the dual-beam antenna samples the precipitating system. This allows the retrieval of all the derivatives, in particular the vertical vorticity, which was not the case in the traditional VAD analysis, nor in the single beam approach of Protat et al. (1997). Simulations have shown that the method was able to retrieve the wind and its first-order derivatives, including the terminal fall velocity of the hydrometeors with satisfying accuracy when the fore and aft antennas form an equal angle with respect to the perpendicular to the aircraft track—that is, with small drift and when the purl is roughly circular and large enough. When this is not the case, errors increase on all parameters. When all sources of errors are considered, typical error values for FASTEX data are 0.2 m s^{-1} on U_0, V_0, 4×10^{-5} to 4×10^{-6} on U_x, U_y, V_x, V_y, (up to 1.5×10^{-4} s^{-1}, i.e., 40% on ROT), 0.1 m s^{-1} on V_f.

The DAVAD analysis has then been applied to a selected FASTEX case, IOP 12 (9 February 1997), characterized by an explosive deepening of a secondary low. A systematic application of DAVAD on all the purls flown during this IOP was performed. Application to real data was possible in spite of the somewhat poor resolution in azimuth of the P3-42 data. Consistent retrieved features are nevertheless identified. The vertical profiles of terminal fall velocity of the hydrometeors were obtained for all the processed purls. In stratiform precipitation areas, they can be used as an a posteriori validation for the whole DAVAD analysis and can be included as input and validation for the models. The retrieved wind field is representative of the area in which it is obtained (warm conveyor belt, cold conveyor belt, dry intrusion) in good agreement with the wind sensor onboard the aircraft, and with the MANDOP-derived winds. The corresponding first-order derivative terms are also consistent: the vertical vorticity, cyclonic, or anticyclonic depending on the location of the purl in the system, is reasonably consistent with that obtained independently using the MANDOP analysis applied at the scale of the cyclone as a whole. Despite the fact that vertical vorticity is determined through a residual term with moderate accuracy (owing mostly to the small purl radii during FASTEX), cyclonic vorticity is found, as expected, with a maximum value at the center of the observed secondary low. The various flows around the secondary low are identified from the horizontal and vertical velocity components and from the deformation profiles, depending on the considered area. The description of the system is consistent with the analysis of Lemaître et al. (1999) done using MANDOP. Moreover, an analysis of the deformation parameters indicates that frontogenesis occurs on the west side of the cloud head, and frontolysis occurs on its east side. This is in agreement with the temperature pattern of Lemaître et al. (1999) who find a baroclinic zone on the western side of the cloud head and a relatively uniform field on its eastern side. The application of DAVAD to other FASTEX IOPs is presently under progress, using particular the ASTRAIA-ELDORA dataset, the resolution of which is twice better than that of the P3-42. Results from IOPs 12 and 16 are readily available to the scientific community in the FASTEX database.

Acknowledgments. FASTEX has been supported by the Programme Atmosphère et Océan à Moyenne Echelle of the Institut National des Sciences de l'Univers under Contract 97/01 and by the European Commission under Contract ENV4-CT96-0322.

REFERENCES

Browning, K. A., and R. Wexler, 1968: The determination of kinematic properties of a wind field using Doppler radar. *J. Appl. Meteor.*, **7,** 105–113.

——, N. M. Roberts, and A. J. Illingworth, 1997: Mesoscale analysis of the activation of a cold front during cyclogenesis. *Quart. J. Roy. Meteor. Soc.*, **123,** 2349–2375.

Bluestein, H. B., 1986: Fronts and jet streaks: A theoretical perspective. *Mesoscale Meteorology and Forecasting.* P. S. Ray, Ed., Amer. Meteor. Soc., 173–215.

Dou, X. K., G. Scialom, and Y. Lemaître, 1996: MANDOP analysis and airborne Doppler radar for mesoscale studies. *Quart. J. Roy. Meteor. Soc.*, **122,** 1231–1261.

Frush, C. L., P. H. Hildebrand, and C. A. Walther, 1986: The NCAR airborne Doppler radar. Part II: System design considerations. Preprints, *23d Radar Meteorology Conf.*, Snowmass, CO, Amer. Meteor. Soc., 151–154.

Heymsfield, A. J., 1978: The characteristics of graupel particles in northeastern Colorado cumulus congestus clouds. *J. Atmos. Sci.*, **35,** 284–295.

Hildebrand, P. H., and C. K. Mueller, 1985: Evaluation of meteorological airborne Doppler radar. Part I: Dual-Doppler analyses of air motions. *J. Atmos. Oceanic Technol.*, **2,** 362–380.

——, C. A. Walther, C. L. Frush, J. Testud, and F. Baudin, 1994: The ELDORA/ASTRAIA airborne Doppler radar: Goals, design, and first field tests. *Proc. IEEE,* **82,** 1873–1890.

Joly, A., and Coauthors, 1997: The Fronts and Atlantic Storm-Track Experiment (FASTEX): Scientific objectives and experimental design. *Bull. Amer. Meteor. Soc.*, **78,** 1917–1940.

Jorgensen, D., P. Bessemoulin, S. Clough, and J. Moore, 1996: Fronts and Atlantic Storm Track Experiment (FASTEX) operation plan. Tech. Rep. 5, FASTEX Project Office, Centre National de Recherches Météorologiques, 164 pp.

——, P. H. Hildebrand, and C. L. Frush, 1983: Feasibility test of an airborne pulse Doppler radar. *J. Climate Appl. Meteor.*, **22,** 744–757.

Lee, W. C., P. Dodge, F. D. Marks, and P. H. Hildebrand, 1994: Mapping of airborne Doppler radar data. *J. Atmos. Oceanic Technol.*, **11,** 572–578.

Lemaître, Y., A. Protat, and D. Bouniol, 1999: Pacific and Atlantic

''bomblike'' deepenings in mature phase: A comparative study. *Quart. J. Roy. Meteor. Soc.,* **125,** 3513–3534.

Locatelli, J. D., and P. V. Hobbs, 1974: Fall speeds and masses of solid precipitation particles. *J. Geophys. Res.,* **79,** 2185–2197.

Mapes, B. E., and R. A. Houze, 1995: Diabatic divergence profiles in western Pacific mesoscale convective systems. *J. Atmos. Sci.,* **52,** 1807–1828.

Matejka, T. J., and R. C. Srivastava, 1991: An improved version of the extended velocity–azimuth display analysis of single-Doppler radar data. *J. Atmos. Oceanic Technol.,* **8,** 453–466.

Protat, A., Y. Lemaître, and G. Scialom, 1997: Retrieval of kinematic fields using a single-beam airborne Doppler radar performing circular trajectories. *J. Atmos. Oceanic Technol.,* **14,** 769–791.

Scialom, G., and J. Testud, 1986: Retrieval of horizontal wind field and mesoscale vertical vorticity in stratiform precipitation by conical scannings with two Doppler radars. *J. Atmos. Oceanic Technol.,* **3,** 693–703.

——, and Y. Lemaître, 1990: A new analysis for the retrieval of three-dimensional mesoscale wind fields from multiple Doppler radar. *J. Atmos. Oceanic Technol.,* **7,** 640–665.

——, and ——, 1994: QVAD: A method to obtain quadratic winds from conical scans by a Doppler weather radar network. *J. Atmos. Oceanic Technol.,* **11,** 909–926.

Srivastava, R. C., T. J. Matejka, and T. J. Lorello, 1986: Doppler radar study of the trailing anvil region associated with a squall line. *J. Atmos. Sci.,* **43,** 356–377.

Testud, J., G. Breger, P. Amayenc, M. Chong, B. Nutten, and A. Sauvaget, 1980: A Doppler radar observation of a cold front: Three dimensional air circulation, related precipitation system and associated wavelike motions. *J. Atmos. Sci.,* **37,** 78–98.

——, P. H. Hildebrand, and W. C. Lee, 1995: A procedure to correct airborne Doppler radar data for navigation errors, using the echo returned from the earth's surface. *J. Atmos. Oceanic Technol.,* **12,** 800–820.

Webster, P. J., and R. Lucas, 1992: The Coupled Ocean–Atmosphere Response Experiment. *Bull. Amer. Meteor. Soc.,* **73,** 1377–1415.